Nonlinear MHD 2007 Q3 Milestones Report

J. Breslau, J. Chen, E. Held, S. Jardin[1], S. Kruger, P. Snyder, C. Sovinec, H. Strauss, and the M3D, NIMROD, and CEMM Teams

June 29, 2007

1. Improve understanding of the present discrepancy between NIMROD and M3D and move to new CDX-U-relevant cases with more realistic parameters and sources.

Q3: Develop an analytically specified equilibrium. Apply NIMROD, M3D and a third code (MARS) for linear growth rate comparisons.

Report:

A method has been developed for analytically specifying an equilibrium configuration similar to CDX-U. We are in the process of agreeing to the exact parameters to use in the NIMROD and M3D calculations, but they will make use of the formalism presented here.

1.1. Derivation of Equations:

Consider the steady-state MHD single fluid resistive equations in the absence of sources:

$$\nabla \times \mathbf{E} = 0 \tag{1}$$

$$\mathbf{E} + \mathbf{V} \times \mathbf{B} = \eta \mathbf{J} \tag{2}$$

$$\nabla \bullet \left[\mathbf{q} + \tfrac{5}{2} p \mathbf{V} \right] = \mathbf{J} \bullet \mathbf{E} \tag{3}$$

$$\nabla p = \mathbf{J} \times \mathbf{B} \tag{4}$$

$$\mu_0 \mathbf{J} = \nabla \times \mathbf{B} \tag{5}$$

Assuming axisymmetry, we write the magnetic field in the normal way in terms of a flux function ψ, the toroidal field function g, and the axisymmetric coordinate ϕ with $|\nabla \phi| = 1/R$:

$$\mathbf{B} = \nabla \phi \times \nabla \psi + g \nabla \phi \tag{6}$$

In steady state, it follows from (1) and (2) that the loop voltage is a spatial constant:

[1] Editor: jardin@pppl.gov

$$V_L = \frac{2\pi\eta\langle \mathbf{J}\bullet\mathbf{B}\rangle}{\langle \mathbf{B}\bullet\nabla\phi\rangle} = \frac{2\pi\eta g}{\mu_0 V'\left\langle \frac{1}{R^2}\right\rangle}\left[\frac{V'}{g}\left\langle\frac{|\nabla\psi|^2}{R^2}\right\rangle\right]_\psi \tag{7}$$

Here brackets denote the standard flux surface average, subscript denotes partial differentiation, and V' is the derivative of the volume within a flux surface with respect to the flux function ψ.

Equations (4)-(6) can be combined to give the Grad-Shafranov equation:

$$R^2\nabla\bullet R^{-2}\nabla\psi + \mu_0 R^2 p' + gg' = 0 \tag{8}$$

Equation (8) can be solved together with (7) for the flux function ψ if we specify boundary conditions (that ψ vanish on some boundary curve) and prescribe the constant V_L and the two surface functions $p(\psi)$ and $\eta(\psi)$. Note that equation (8) can be surface averaged and combined with (7) to give another relation useful for obtaining the toroidal field function g.

$$\tfrac{1}{2}(g^2)'\left[1-\left\langle\frac{|\nabla\psi|^2}{R^2}\right\rangle\Big/\left\langle\frac{1}{R^2}\right\rangle g^2\right]+\left[\frac{\mu_0 V_L}{2\pi\eta}+\mu_0 p'\Big/\left\langle\frac{1}{R^2}\right\rangle\right]=0 \tag{7'}$$

It follows from (3) and (2) that in steady state, the surface averaged energy equation takes the simple form:

$$V_L\frac{dK}{d\psi}+\frac{dQ}{d\psi}=0 \tag{9}$$

Here the surface averaged integrated current density is

$$K = \frac{V'}{2\pi\mu_0}\left\langle\frac{|\nabla\psi|^2}{R^2}\right\rangle \tag{10}$$

and the surface averaged total heat flux is:

$$Q = V'\left[\langle \mathbf{q}\bullet\nabla\psi\rangle + \tfrac{5}{2}\,p\Gamma\right] \tag{11}$$

We have introduced the particle flux corresponding to collisional Pfirsch Schluter diffusion:

$$\Gamma \equiv \eta\left[\left\langle R^2\mathbf{J}\bullet\nabla\phi\right\rangle - \frac{\left\langle \mathbf{J}\bullet\mathbf{B}\right\rangle}{\left\langle \mathbf{B}\bullet\nabla\phi\right\rangle}\right]$$
$$= -\eta p'\left\langle\frac{\left|\nabla\psi\right|^2}{B^2}\right\rangle\left[1+g^2\left\langle\frac{\left|\nabla\psi\right|^2}{B^2}\right\rangle^{-1}\left(\left\langle B^{-2}\right\rangle - \left\langle B^2\right\rangle^{-1}\right)\right] - \frac{1}{2\pi}V_L\left[1-\left\langle\frac{B_T^2}{B^2}\right\rangle\right] \tag{12}$$

(The second relation is derived in [2]). Let the random heat flux be given by $\mathbf{q} = -\chi 2nk_B\nabla T = -\chi 2nk_BT'\nabla\psi$. Since V_L is a constant, we can integrate (9) to obtain:

$$\chi = \frac{1}{2nk_BT'\left\langle\left|\nabla\psi\right|^2\right\rangle}\left[\frac{V_L}{2\pi\mu_0}\left\langle\frac{\left|\nabla\psi\right|^2}{R^2}\right\rangle + \tfrac{5}{2}\,p\Gamma\right] \tag{13}$$

The second term in brackets in Eq. (13) is the convective term due to classical diffusion and will be neglected in the following. It is assumed to be much smaller than the first term.

1.2 Boundary and Profile Specification

1. The *plasma boundary* is parameterized with the 4 scalar variables (R_0, a, κ,δ) as follows:

$$R(\theta) = R_0 + a\cos[\theta + \delta\sin(\theta)]$$
$$Z(\theta) = a\kappa\sin(\theta) \tag{14}$$

2. The *temperature profile* is taken to be linear in the normalized poloidal flux with central value T_0:

$$T(\psi) = T_0\tilde{\psi} \tag{15}$$

3. Here, the *normalized poloidal flux* is defined relative to the axis value ψ_A and the limiter value ψ_L, which are in turn determined by the equilibrium solution:

$$\tilde{\psi} \equiv \frac{(\psi - \psi_L)}{(\psi_A - \psi_L)} \tag{16}$$

4. The *pressure profile* depends on the 2 scalar constants p_0 and α:

$$p(\psi) = p_0\left[\alpha\tilde{\psi} + (1-\alpha)\tilde{\psi}^2\right] \tag{17}$$

5. The *density* and *resistivity* profiles are determined in terms of the pressure and temperature as follows:

$$n(\psi) = p(\psi)/2k_BT(\psi) \tag{18}$$

$$\eta(\psi) = C_1[T(\psi)]^{-3/2} \tag{19}$$

with $k_B = 1.6022 \times 10^{-19}$ J/ev and $C_1 = Z_{EFF} \times 1.03 \times 10^{-3}$ Ω-m (assumes $ln\Lambda$=20). Note that this gives a central and edge electron density of:

$$n_0 = \frac{p_0}{2k_B T_0}, \qquad n_e = \alpha n_0 \tag{20}$$

6. The toroidal field is determined by integrating Equations (7) when the boundary value g_0 and the loop voltage V_L are specified. It is sometimes useful to specify the loop voltage in terms of the approximate central safety factor q_0:

$$V_L = \frac{4\pi g_0 C_1}{\mu_0 q_0 R_0} T_0^{-3/2} \tag{21}$$

1.3 Input Parameters:

In defining the standard equilibrium, we used the following parameters:

var	value	definition	comment
R_0	0.341 m	Major radius	Eq. 14
a	0.247 m	Minor radius	"
κ	1.35	ellipticity	"
δ	0.25	triangularity	"
T_0	100 eV	Central Temperature (Te = Ti)	Eq. 15
$\mu_0 p_0$	2.5 E-4	Central pressure × μ_0	Implies $n_0 = 1.8 \times 10^{19}$ m^{-3}
α	0.1	Parameter in pressure equation	Implies $n_e = 1.8 \times 10^{18}$ m^{-3}
g_0	0.042 T-m	Vacuum value of $R \times B_T$	
Z_{EFF}	2.0	Effective Charge	
V_L	3.1741 V	Loop Voltage	From (21) implies q_0~0.8

1.4 Results

The computed equilibrium had plasma current Ip = 44.4 kA, q(0) = 0.81. The χ profile, as determined by Eq. (13), varied from 12.35 m^2/s on axis to 118.8 m^2/s at the edge.

References for this section:

[1] S. P. Hirshman and S. C. Jardin, "Two-dimensional transport of tokamak plasmas", Phys. Fluids 22 731 (1979)
[2] S. Jardin, "On Pfirsch-Schluter flows in MHD codes", http://w3.pppl.gov/cemm/Project/Pfirsch-Schluter.pdf
[3] S. C. Jardin, "Lecture notes for AST 560: Computational Methods in Plasma Physics, Princeton University Spring 2007"

2. Perform a linear edge stability calculation in a non-diverted equilibrium with a resistive code, and compare results with the linear ideal MHD code ELITE.

Q3. Repeat Q2 with equilibria that is closer to the threshold values.

Report:

2.1 Progress on ELM Benchmarking of ELITE and Extended MHD Codes:
In the Q2 milestone report, we reported on the development of an inverse equilibrium suitable for use by nonlinear, initial value codes. The equilibrium used is an inverse equilibrium with a "vacuum region" inside. The pressure profile is flat in the core to avoid pressure-driven core instabilities. The current at the edge includes the self-consistent bootstrap current using the Sauter model. The pedestal width given is approximately 10% of the normalized poloidal flux, which is approximately twice the normal experimental width. This was done to try and minimize the effects of the transition region from low resistivity to high resistivity for the initial value codes.

As expected, GATO and ELITE give excellent agreement with the equilibrium as shown in Figure 1. The unique growth rate spectrum is due to the rational q's which are near the surface, and is indicative of a strong peeling component in this case. GATO was run with and without a wall at $r_{wall}/a=1.8$ to give an indication of the importance of wall stabilization. For this equilibrium, the wall is a relatively unimportant effect.

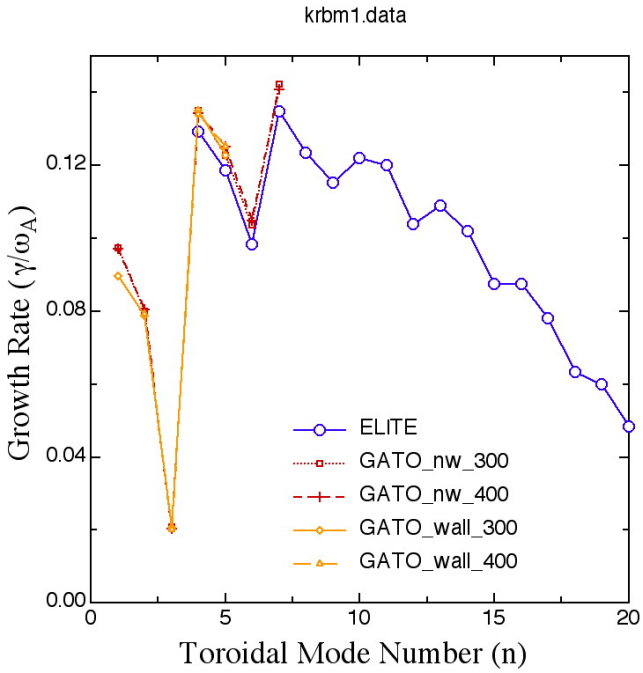

Figure 1. ELITE and GATO give excellent agreement for this result. The rapidly varying mode spectrum indicates the presence of a rational surface near the vacuum region (in this case, q=3) and a strong peeling component.

2.2 NIMROD Computational Results:

NIMROD has begun preliminary studies with this equilibrium. The initial results are shown in Figure 2. These cases were performed at values of $S=10^5$ in the core, and $S=10^2$ in the vacuum region, with the location of the transition region at x=0.78 versus the location of the vacuum region of x=0.755 (where x is the normalized poloidal flux). The growth rates are of the right magnitude, but the edge resonance is not detected for the parameters used.

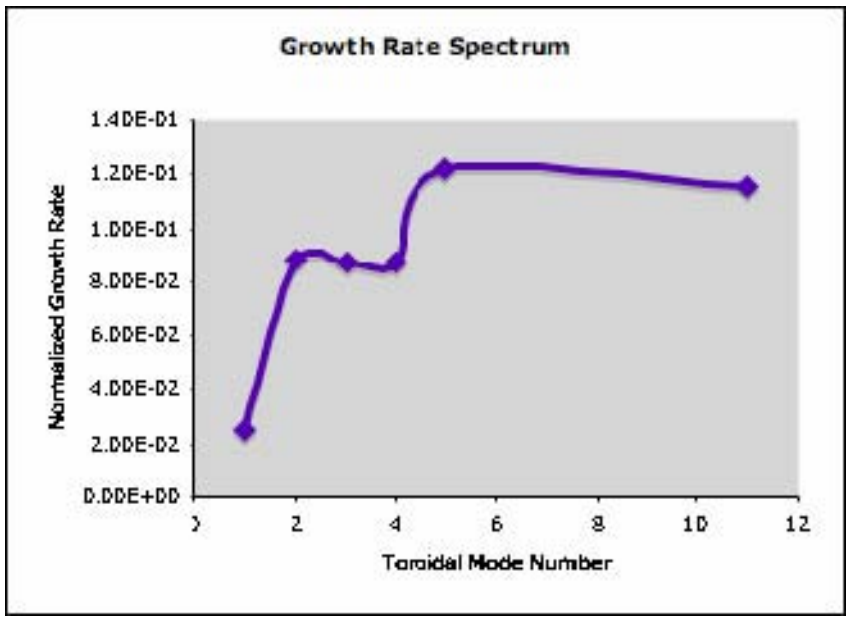

Figure 2. Preliminary growth rates from NIMROD show the correct order of magnitude, but do not show the sensitivity to the edge resonance condition.

The eigenfunctions show excellent agreement as shown in Figure 3 indicating that the correct modes are being found, if the growth rates do not yet have quantitative agreement.

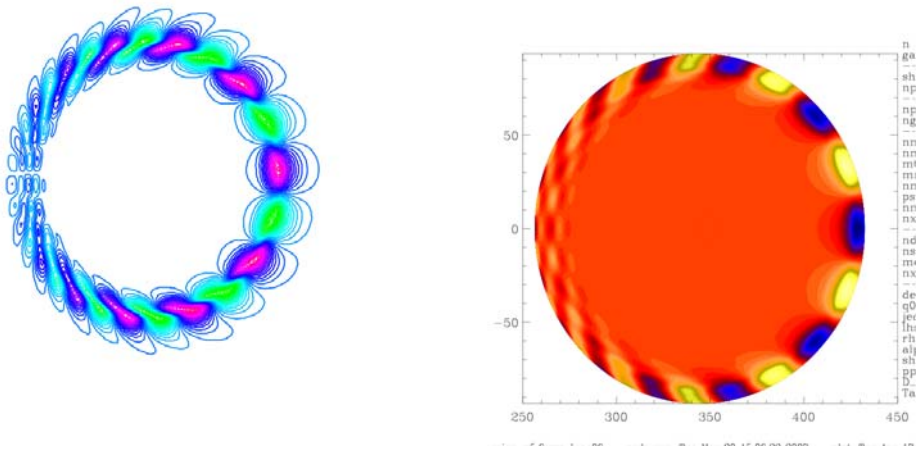

Figure 3. The n=5 eigenfunction from NIMROD (left) and ELITE (right) show excellent agreement.

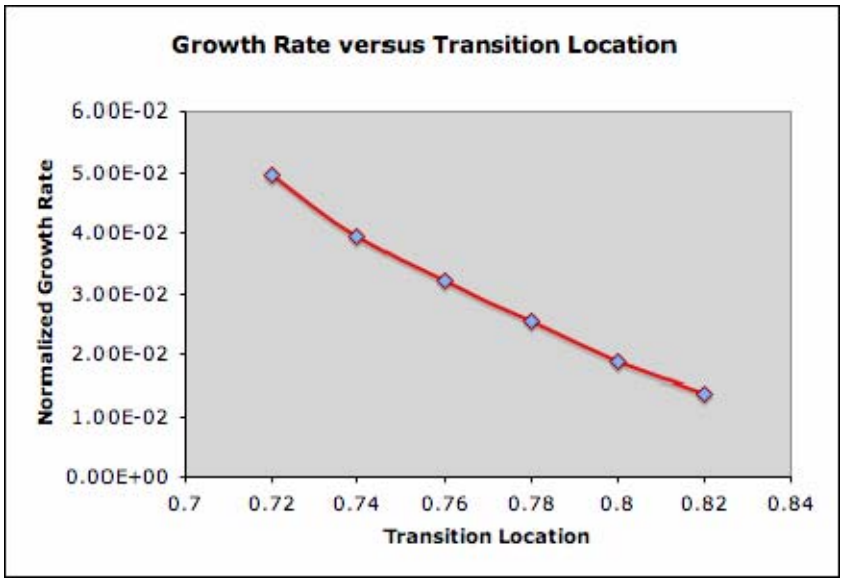

Figure 4. The growth rate results are sensitive to the location of the resistive transition region. Here, the n=1 growth rate shows a 33% change in growth rate for a 2% change in transition location (note the the vacuum is located at x=0.755).

To converge to the ideal result, the nonideal codes need to asymptotically take the resistivity in the core to zero, and the resistivity in the vacuum to infinity. An important part in taking this limit is to explore the sensitivity of the growth rates to this transition. A measure of this sensitivity can be seen in examining the sensitivity of the growth rate to the location of the transition region. This is seen in Figure 4. The results show that for the n=1 mode, the results are sensitive to the location of the transition region indicating that converging to the ideal results is going to be challenging. Work on this equilibrium is continuing.

The motivation for converging the non-ideal codes to the artificial ideal limit is the success of ELITE in predicting the stability boundaries of the experimental measurements of Type I ELMs, and in predicting the width of the modes. To this end, the ultimate goal is to understand how the prediction of the stability boundaries predicted by the non-ideal codes compares to the ideal codes. We will report on these efforts in the next milestone.

2.3 M3D Computational Results:

The M3D code has been applied to the equilibrium described in Figure 1. The results of that study are summarized in Figure 5:

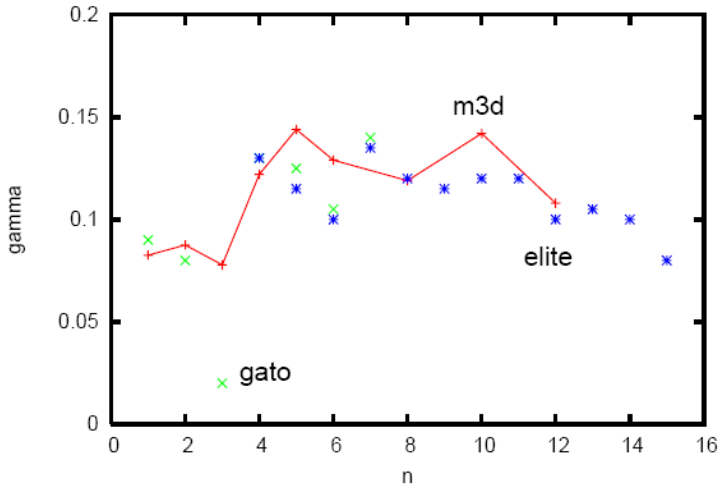

Figure 5 M3D linear growth rates compared to ELITE and GATO

We find that the M3D linear growth rates comparable to ELITE and GATO for $\eta_{inner}= 10^{6}$, $\eta_{outer}=10^{-2}$. However, the results are somewhat sensitive to the values and profiles of resistivity, and these are of course not in the ELITE model. For the purpose of this comparison, 2-fluid and flow effects were absent

2.4 Progress on Closures used for ELM Simulations:

An analytic derivation of general, time-dependent parallel closures for electron and ion heat flows and stresses is underway. Such closures will be useful in simulations of edge phenomena where the short (relative to resistive time scales) growth times of edge localized modes demand that the time derivative is kept in the kinetic equation. Importantly, these closures provide physical dissipation in the fluid model including Landau damping, presumably important near the top of the edge pedestal, and accurate collisional effects, important near the bottom of the pedestal. In addition to providing much needed smoothing of the fields in nonlinear simulations, such dissipation may be crucial to determining the nonlinear saturation and regulation mechanism of ELMs.

The time-dependent theory follows that of Chang and Callen with some important improvements. First, the linearized collision operator which uses a moment expansion yields quantitative results in the collisional limit. Second, the initial condition for the distribution function and its influence on the closures is retained in the theory. And finally, nonlinear effects due to perturbed density and temperature are retained.

This final improvement is critical in light of the existing nonlinear ELM simulation results which exhibit substantial perturbation to the background fields.

3. Extend the 2D GEM nonlinear benchmark to non-zero guide field and more extreme parameters.

Q3: Perform comparative study of non-zero guide field sequence

Report:

3.1 Problem Specification:

What has become a "standard problem" in 2-fluid magnetic reconnection was proposed in [1]. We define an initial equilibrium in 2D slab geometry as follows;

$$\begin{aligned}
&\text{Poloidal Magnetic Flux: } \psi^0(x,y) = \frac{1}{2}\ln\left(\cosh 2y\right) \\
&\text{Toroidal Field: } I^0(x,y) = B^0 \\
&\text{Total Pressure: } P^0(x,y) = \frac{1}{2}\left[\operatorname{sech}^2(2y) + 0.2\right] \\
&\text{Electron Density: } n^0(x,y) = \left[\operatorname{sech}^2(2y) + 0.2\right] \\
&\text{Electron Pressure: } P_e^0(x,y) = 0.2P^0(x,y)
\end{aligned} \tag{3.1}$$

All other quantities are initialized to zero. A perturbation in the poloidal flux is applied at time *t=0* as follows:

$$\psi(x,y) = \varepsilon \cos k_x x \cos k_y y\,. \tag{3.2}$$

The initial equilibrium and perturbed current densities are just the Laplacian of the fluxes, $J^0 = \nabla^2\psi^0, J = \nabla^2\psi$. The computation is carried out in a rectangular domain: $-L_x/2 \le x \le L_x/2$ and $-L_y/2 \le y \le L_y/2$. The system is taken to be periodic in the *x*-direction with ideal conducting boundaries at $y = \pm L_y/2$. The parameters are chosen such that $k_x = 2\pi/L_x$, $k_y = \pi/L_y$, with $L_x = 25.6$, $L_y = 12.8$, and $\varepsilon = 0.1$.

3.2 M3D-C^1 Results

The reconnection calculations presented here extend the GEM [1-2] reconnection problem to include a strong background (guide) magnetic field B^0 as is present in a fusion plasma. We find that the background field significantly delays the onset of the fast reconnection phase and reduces the maximum reconnection rate and the amplitude of the velocities that develop in the reconnection region. This is illustrated in Figures 6-7. The nominal values of resistivity and viscosity are η=0.005 and μ=0.005.

The curves in Figure 6 show the reconnected flux, the magnetic reconnection rate, and the kinetic energy as a function of time for the GEM problem defined above, but with different values of the background toroidal field: 0.2, 1.0, 2.0, and 5.0. It can be seen that the case with B^0 = 0.2 exhibits a fast reconnection phase which is very similar in structure and in magnitude to the B^0 = 0 case presented in [2]. However, as B^0 is increased to 1.0, 2.0 and then to 5.0 and beyond, the onset time of the fast reconnection phase is delayed substantially and the maximum rate is significantly reduced.

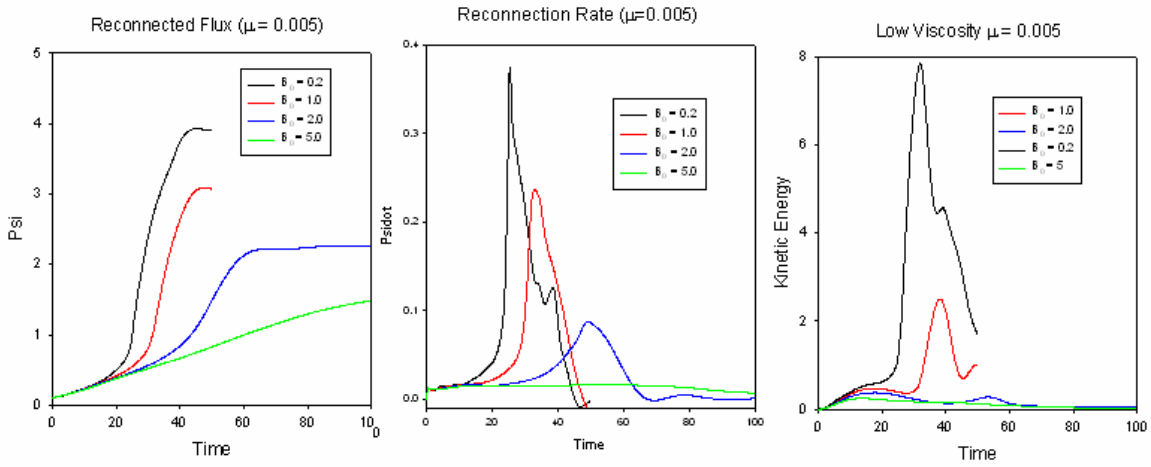

Figure 6: Reconnected flux, reconnection rate, and kinetic energy vs. time for GEM reconnection case with different guide fields.

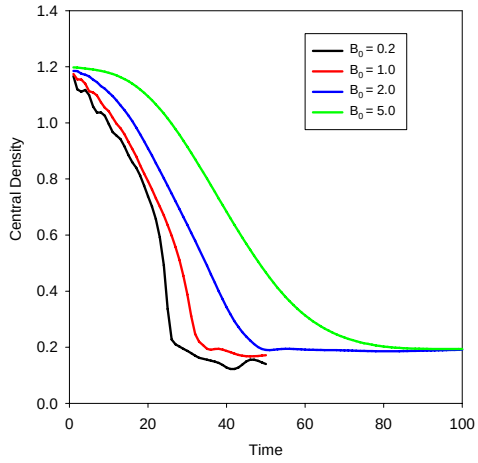

Figure 7 Central density vs. time for different guide fields.

In Figure 7 we plot the density at the reconnection point as a function of time for the four cases of Figure 1a. It is seen that as the toroidal field increases and the solution becomes more like the incompressible solution, the density at the center (reconnection region) decreases much slower to the far-field value.

3.3 NIMROD Results

Qualitatively similar results are found by NIMROD when comparing the reconnection with and without a guide field. Figures 8 and 9 show very recent results comparing the no guide field case and the guidefield = 1 case. The parameters are: electrical diffusivity = 5.e-3, artificial particle diffusivity = 5.e-5 (10X smaller than previous), viscosity=therm diffusivity = 5.e-2, electron mass = 1/100 of ion mass. It can be seen that the $B_{guide} = 1$ case reconnects substantially slower than the $B_{guide} = 0$ case, and that the kinetic energy is greatly suppressed.

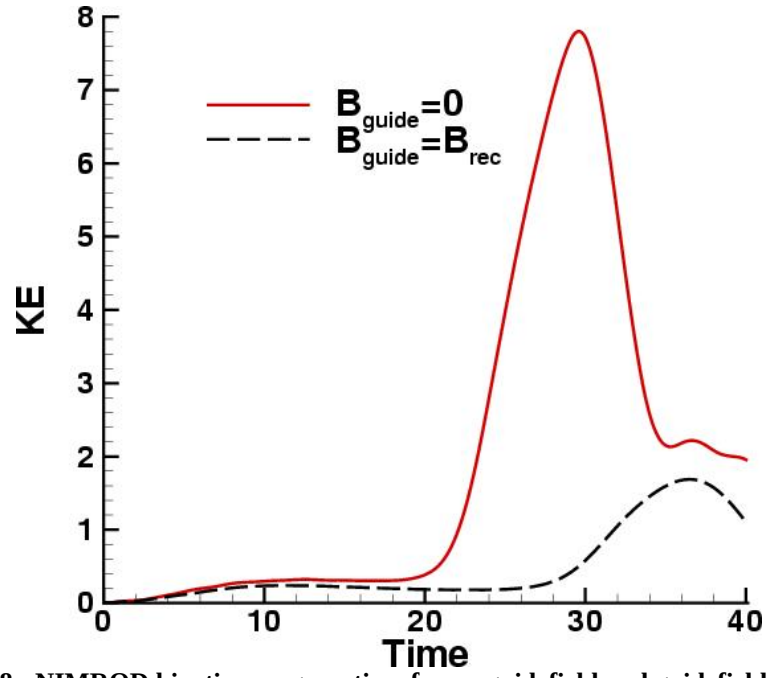

Figure 8: NIMROD kinetic energy vs time for no guidefield and guidefield=1 cases

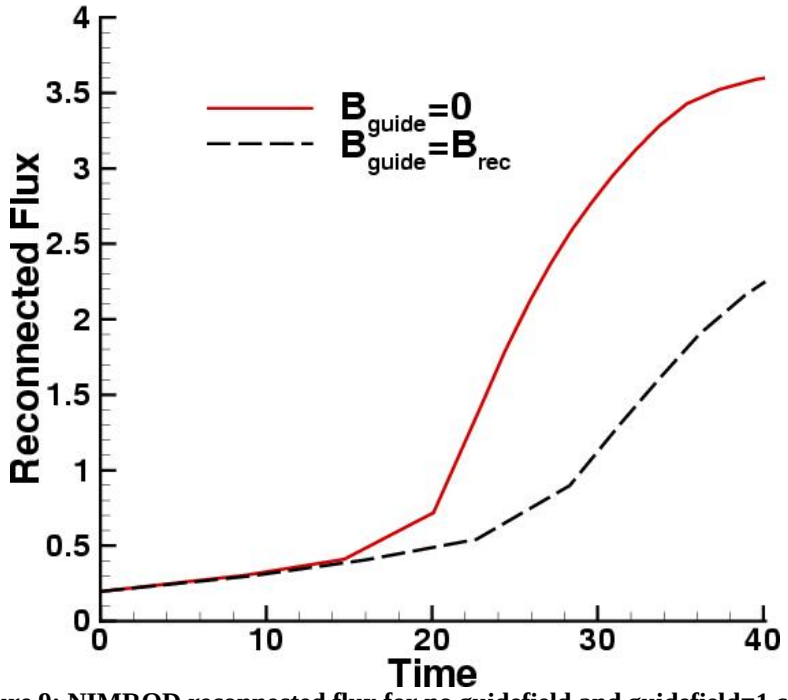

Figure 9: NIMROD reconnected flux for no guidefield and guidefield=1 cases

3.4 Discussion

The explanation for the marked difference between the low (or zero) and high guide-field cases has to do in part with the evolution of the plasma density as shown in figure 7. In the zero or low guide field cases, the compressibility of the flow causes the density to quickly deplete in the reconnection region, increasing the effect of the Hall term and thereby accelerating the reconnection. The faster the fluid reconnects, the lower the density at the reconnection point becomes, and thus the sudden shock-like transition. As the guide field is increased, the fluid is forced to become more incompressible, removing this effect and thus greatly decreasing the maximum reconnection rate. However, it is clear that the density evolution alone cannot explain the differences in the reconnection rates, as we see from Figure 6 that the B^0=5 case eventually reaches the same low density as the B^0=0.2 case, but the reconnection rate never reaches that of the lower guidefield case.

References for this section

[1] Birn, et al, J. Geophys Res **106**, 3715 (2001)

[2] S. C Jardin, J. Breslau, and N. Ferraro, PPPL-4209, (to appear in J. Comp. Phys.) (2007)

4. Scalability studies on leading edge computers.

Q3: Repeat scaling studies for improved performance

Report:
M3D is now fully functional and runs efficiently on the whole machine (5120 nodes, 10,240 processors) of the Jaguar Cray XT3 computer at ORNL. Impressive weak and strong scaling results have been obtained using only one of the two processor cores on each node. Excess of 60-80% overall efficiency was observed when going from 64 to 5120 nodes. This result was obtained using the "Hypre" algebraic multigrid solver within PETSc for solving the compute intensive linear equations in M3D each timestep that arise from the elliptic equations. More details of the scaling results can be found at http://w3.pppl.gov/m3d/scale.html.

NIMROD has obtained very favorable parallel scaling results in problems where the parallel closures dominate the running time. They have demonstrated over 70% efficiency in strong scaling in going from 1024 to 2048 to 4096 processors on Seaborg. More details can be found at http://w3.pppl.gov/CEMM/Sherwood2007/Held.pdf